AGU ADVANCING EARTH AND SPACE SCIENCE

Geophysical Research Letters®

RESEARCH LETTER
10.1029/2021GL094376

Key Points:

- Wind forced near-inertial waves and internal tides can efficiently drain oceanic mesoscale eddy energy
- Eddy energy "draining" is largely a result of an internal-wave induced modifications to the turbulent energy cascades
- The strongest forward energy transfers are found in submesoscale fronts and filaments that dynamically depart from geostrophic balance

Supporting Information:

Supporting Information may be found in the online version of this article.

Correspondence to:

R. Barkan,
rbarkan@tauex.tau.ac.il

Citation:

Barkan, R., Srinivasan, K., Yang, L., McWilliams, J. C., Gula, J., & Vic, C. (2021). Oceanic mesoscale eddy depletion catalyzed by internal waves. *Geophysical Research Letters*, *48*, e2021GL094376. https://doi.org/10.1029/2021GL094376

Received 23 MAY 2021
Accepted 8 SEP 2021

Oceanic Mesoscale Eddy Depletion Catalyzed by Internal Waves

Roy Barkan[1,2], Kaushik Srinivasan[2], Luwei Yang[2], James C. McWilliams[2], Jonathan Gula[3,4], and Clément Vic[3]

[1]Porter School of the Environment and Earth Sciences, Tel Aviv University, Tel Aviv, Israel, [2]Department of Atmospheric and Oceanic Sciences, University of California, Los Angeles, CA, USA, [3]Laboratoire d'Océanographie Physique et Spatiale, Université de Bretagne Occidentale, Plouzané, France, [4]Institut Universitaire de France (IUF), Paris, France

Abstract The processes leading to the depletion of oceanic mesoscale kinetic energy (KE) and the energization of near-inertial internal waves are investigated using a suite of realistically forced regional ocean simulations. By carefully modifying the forcing fields we show that solutions where internal waves are forced have ∼25% less mesoscale KE compared with solutions where they are not. We apply a coarse-graining method to quantify the KE fluxes across time scales and demonstrate that the decrease in mesoscale KE is associated with an internal wave-induced reduction of the inverse energy cascade and an enhancement of the forward energy cascade from sub-to super-inertial frequencies. The integrated KE forward transfer rate in the upper ocean is equivalent to half and a quarter of the regionally averaged near-inertial wind work in winter and summer, respectively, with the strongest fluxes localized at surface submesoscale fronts and filaments.

Plain Language Summary Oceanic eddies contain most of the kinetic energy in the ocean and therefore play an important role in determining the ocean's response to future climate scenarios. Oceanic wind- and tidally forced internal waves are energetic fast motions that contribute substantially to the vertical mixing of water, thereby affecting biogeochemical and climate processes. This work shows for the first time in high-resolution, realistically forced, numerical simulations that wave motions can drain a substantial amount of eddy energy by altering the way in which energy is transferred across scales. This has important implications to ocean energetics and to climate models that often lack the resolution and forcing components to represent these wave-induced effects.

1. Introduction

The general circulation of the ocean is strongly constrained by the pathways that kinetic and available potential energy take from the basin-scale forces that inject them to centimeter scales, where they are depleted. To determine the ocean's response to future climate scenarios, these energy pathways, from forcing to dissipation, must be understood and quantified.

Mesoscale eddies, with horizontal scales on the order of 100 km and timescales longer than many days, are well known as the dominant reservoir of kinetic energy (KE) in the oceans (Wunsch & Ferrari, 2004). But because their dynamics are constrained by an approximate geostrophic and hydrostatic force balance, they are characterized by an inverse KE cascade, and by themselves do not provide the necessary forward scale-transfer to dissipation (Müller et al., 2005). Possible mechanisms to interrupt the mesoscale inverse cascade include interaction with the bottom topography and boundary layer (Arbic et al., 2009; Nikurashin et al., 2013; Sen et al., 2008; Trossman et al., 2013, 2016) and instabilities that are strongly linked to the formation of the more rapidly evolving submesoscale currents, with time scales on the order of a day and with horizontal scales of about 0.1–10 km (Capet et al., 2008a; McWilliams, 2016).

Near-inertial waves (NIWs) are predominately storm-forced internal waves with an intrinsic frequency close to the local Coriolis frequency at their generation site and with horizontal scales that are initially as large as the storms that excited them (Alford et al., 2016). Mooring observations indicate that they are a significant mode of high-frequency variability in the ocean (Wunsch & Ferrari, 2004) with a comparable power input on the global scale as internal tides (Alford, 2003; G. Egbert & Ray, 2000). They are characterized by strong

vertical shear (Alford et al., 2017; Pinkel, 2014) and are therefore expected to contribute to upper-ocean mixing, thereby affecting a variety of processes like biogeochemistry and climate (Jochum et al., 2013). Observational estimates of the wind-work that excites NIWs depend on the estimating method and resolution of the wind product, and have global values ranging between 0.3 and 1.3 TW (Alford, 2020; Jiang et al., 2005). This uncertainty emphasizes the difficulty in quantifying NIW energetics in measurements.

In recent years, a growing number of theories and idealized numerical simulations of varying complexity have demonstrated that geostrophic mesoscale eddies and NIWs can interact and exchange energy (Barkan et al., 2017; Bühler & McIntyre, 2005; Polzin, 2010; Rocha et al., 2018; Taylor & Straub, 2016, 2020; J. Thomas & Daniel, 2020; L. N. Thomas, 2017; Wagner & Young, 2016; Whitt & Thomas, 2015; Xie & Vanneste, 2015). These interactions, which are hypothesized to have important implications to both mesoscale KE dissipation routes and to NIW energetics, are however poorly constrained in realistic settings.

Here, we attempt for the first time to quantify NIW-eddy interactions in a series of realistically forced numerical simulations that are validated against mooring-, satellite-, and Argo-based measurements. By comparing numerical simulations with and without externally forced NIWs and internal tides we show that solutions with internal wave (IW) forcing have roughly 25% less mesoscale KE than solutions without IW forcing during both winter and summer months. This decrease in mesoscale KE is associated with an IW-induced reduction in the inverse KE cascade to sub-inertial frequencies and an increase in the forward cascade to super-inertial frequencies. Hereinafter, we refer to these IW-induced modifications to the turbulent cascades as *stimulated* cascades. The strongest forward KE transfer rate is shown to be most prominent in the mixed layer during winter, to be spatially localized in regions of strong submesoscale fronts and filaments that dynamically depart from geostrophic balance, and to have magnitudes comparable to the averaged near-inertial wind work in the study region.

2. Modeling and Validation

Numerical simulations were carried out using the Regional Oceanic Modeling System (ROMS; Shchepetkin & McWilliams, 2005) forced by the Climate Forecast System Reanalysis (CFSR) atmospheric product (Dee et al., 2014), with gradual nesting to zoom in on the Iceland Basin (Figure 1a; Supporting Information S1-Modeling). This region has complex current-topography interactions (Fratantoni, 2001), a rich mesoscale eddy field (Jakobsen et al., 2003), strong NIW activity (Chaigneau et al., 2008), and is the target location for the Near-Inertial Shear and Kinetic Energy in the North Atlantic experiment (L. Thomas et al., 2020).

The presented analysis is based on three simulation sets with 2 km and 500 m horizontal grid spacing. The first set (high-frequency forcing; herein after HF) is forced by hourly winds, hourly boundary conditions from the parent 6 km solution, and includes TPXO-based (G. D. Egbert & Erofeeva, 2002; G. D. Egbert et al., 1994) barotropic tidal forcing at the boundary. The second set (smooth forcing; herein after SM) has no tidal forcing, and the high frequency component of the wind forcing and boundary conditions are removed, using a low-pass filter with a one-day width, to eliminate IWs. The third set (no tidal forcing; herein after NT) has hourly wind- and boundary-forcing but no tidal forcing, and is only simulated on the 2 km grid. The outermost nest is run for three years beginning on January 1, 1999 with the first two years used for spin-up and only the last year used to force the finer nests. All simulation sets are subsequently run for a full year beginning on January 1, 2001. We focus our analysis on winter months (January, February, and March) and summer months (July, August, and September) and use hourly output fields.

Because our modeling approach has no data assimilation our solutions should be viewed as realistic process studies and validation against data can only be done in a statistical sense. With that in mind, the model's annual-mean mesoscale geostrophic eddy kinetic energy at the surface compares well with the Archiving, Validation, and Interpretation of Satellite Oceanographic (AVISO) data set (Figures 1c and 1d; Supporting Information S1-Comparison with measurements), where measured monthly data spanning 1992–2009 is used. Similarly, the horizontally and seasonally averaged stratification in the model compare well with Argo-based measurements, which span 2005–2019 (Figure 1b; Supporting Information S1-Comparison with measurements), although in winter the model is somewhat more stratified than the observations. The

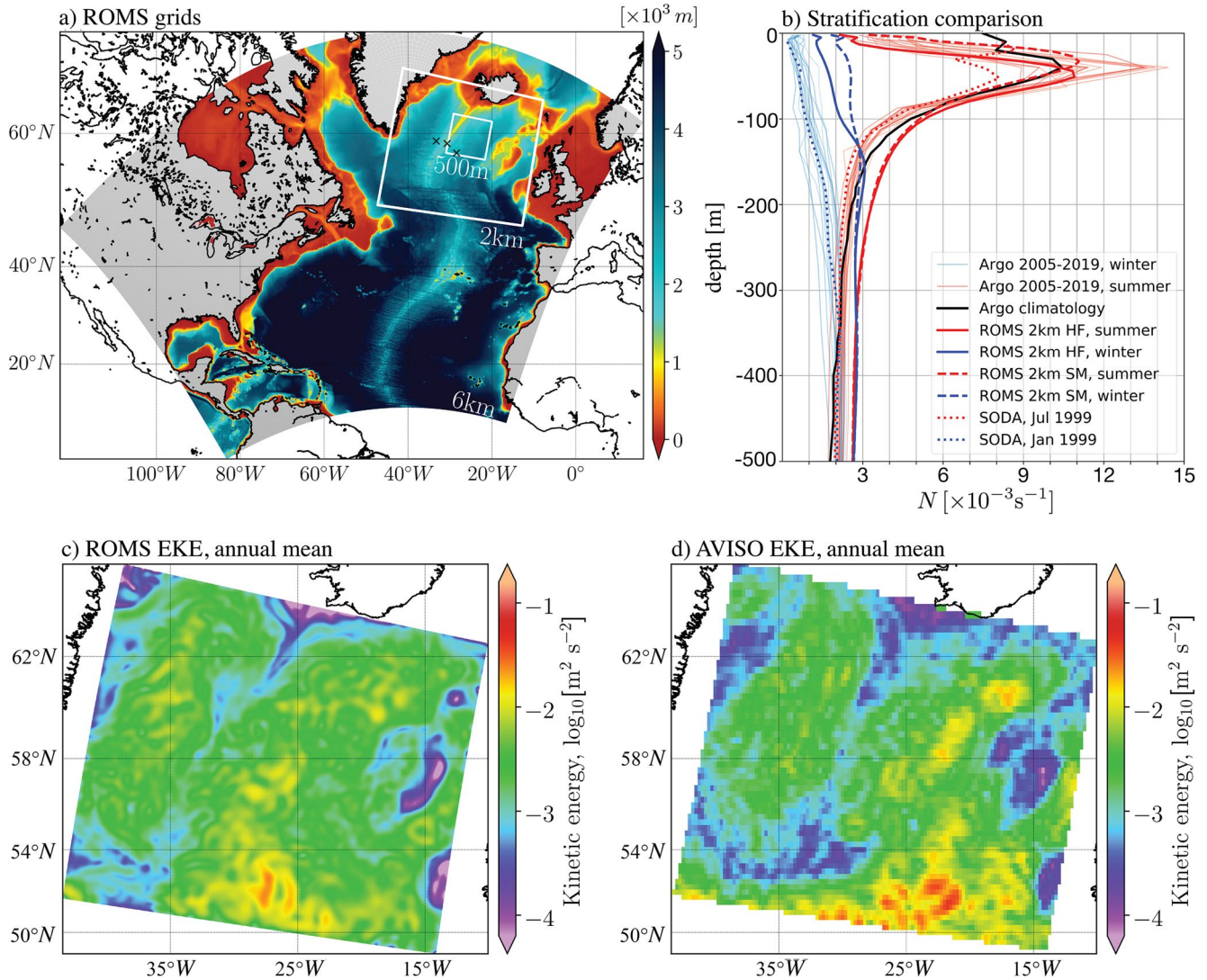

Figure 1. (a) The regional oceanic modeling system (ROMS) grids used in this study (6 km, 2 km, and 500 m horizontal grid spacing) with colors showing bathymetry and markers indicating mooring locations. (b) Horizontally and seasonally averaged stratification comparison between the ROMS 2 km solutions (thick solid and dashed red and blue lines), Argo-based profiles during 2005–2019 (thin solid red and blue lines), Argo annual climatology from the world-ocean atlas (solid black line), and the simple ocean data assimilation (SODA) product (dotted red and blue lines) used to initialize the 6 km solution. (c) ROMS 2 km high-frequency forcing (HF) solution-based and (d) AVISO-based annual mean surface geostrophic eddy kinetic energy (EKE; where "eddy" denotes a perturbation from annual mean), displayed with a log-scale colorbar. The horizontal mean and standard deviation of EKE based on archiving, validation, and interpretation of satellite oceanographic (AVISO) data from 1992 to 2009 is $3.41 \pm 0.47 \times 10^{-3} m^2 s^{-2}$ and based on ROMS from 2001 is $3.18 \pm 0.27 \times 10^{-3} m^2 s^{-2}$. HF and smooth forcing (SM) denote solutions with and without internal wave (IW) forcing, respectively. Further information about the data product and methods is provided in Supporting Information S1-Comparison with measurements.

averaged stratification from the Simple Ocean Data Assimilation (SODA; Carton & Giese, 2008) product used to initialize the coarsest solution is also shown for reference (dotted red and blue lines in Figure 1b).

To further examine how well the model captures the KE distribution as a function of time scales and depth we compare the model power spectral densities (Figure 2) with mooring based measurements (crosses in Figure 1a, Supporting Information S1-Comparison with measurements), which were collected during the Reykjanes Ridge Experiment (Vic et al., 2021). Considering the differences in measured versus simulated years, the model captures well the observed low-frequency (mesoscale) variability as well as the near-inertial and semidiurnal tidal peaks (solid and dashed red lines in Figure 2), which are the main focus of this manuscript. The submesoscale-currents' energy levels (time scales of about a day) are also well represented, particularly in the 500 m nest (dashed red lines in Figure 2). The model, however, underestimates the IW

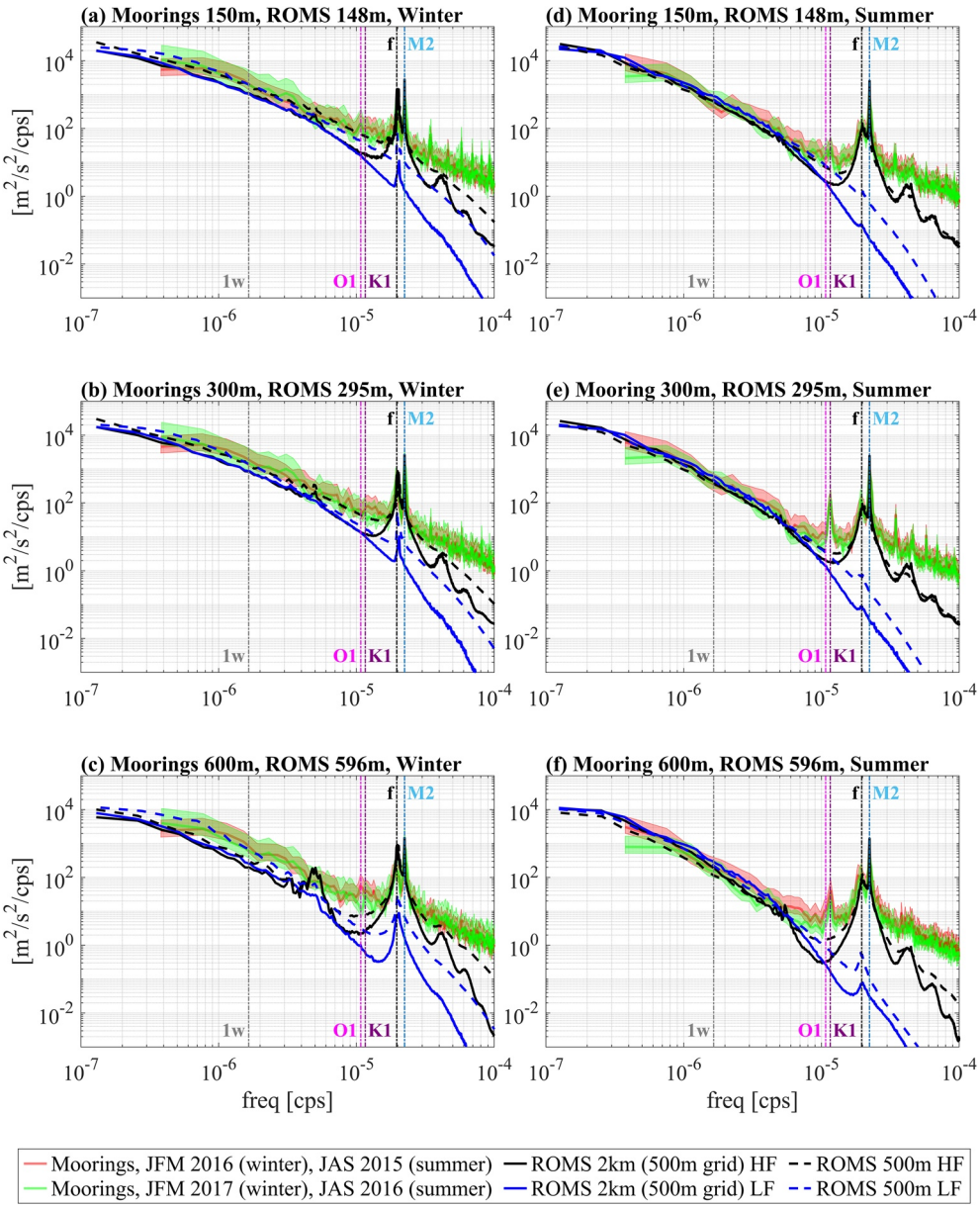

Figure 2. Power spectral densities of horizontal velocities from the mooring data and from the regional oceanic modeling system (ROMS) 2 km and 500 m solutions computed during winter (panels a–c) and summer (panels d–f), at three different depths. The mooring-based spectral densities (black and blue lines) use five overlapping segments with a 50% overlap and are averaged between the three moorings (markers in Figure 1a) separately for each season, where the shading denotes the 95% confidence interval (Supporting Information S1 Comparison with measurements). The ROMS-based spectral densities for both the 2 km and 500 m solutions are averaged over the region occupied by the 500 m grid (Figure 1a). The vertical dashed lines denote one week (1w), the diurnal and semi-diurnal tidal constituents (O1, K1, and M2), and the inertial frequency (f). High-frequency forcing (HF) and smooth forcing (SM) denote solutions with and without internal wave (IW) forcing, respectively.

continuum energy, probably due to the lack of vertical and horizontal resolution and/or the exclusion of remotely generated internal tides (Nelson et al., 2020). The model is also missing a diurnal tidal peak during summer at depth (Figures 2e and 2f), which is presumably associated with the near-ridge dynamics. We do not expect these discrepancies to influence our results, which are focused on the bulk eddy-IW energy exchanges in this region.

3. Cross-Scale Energy Transfers

The frequency spectra of the SM 2 km and 500 m solutions show a substantial energy reduction in time scales shorter than a day compared with HF solutions during both winter and summer (red and green lines in Figure 2), as expected from solutions that lack IW forcing. In addition, a closer look at the frequency spectra at mesoscale time scales (of order 7–14 days; Supporting Information S1 Comparison with measurements) reveals a reduction in energy levels in the HF solutions compared with the SM solutions, at both resolutions. Using a one-week filter cutoff, the seasonal- and volume-averaged low-passed KE in the 2 km HF solution are 12% and 16% less than in the 2 km SM solution in winter and summer, respectively. The reduction in low-passed KE in the 500 m HF solution in both seasons increases to about 24% compared with the 500 m SM solution. We compared the domain averaged low-passed wind work between the HF and SM solutions and found little differences, with a somewhat larger low-passed wind input in the HF solutions (Supporting Information S1 Energetics). This verifies that the reduction in mesoscale KE is not related to differences in the atmospheric forcing. Furthermore, the mesoscale KE estimates above are computed over the region occupied by the 500 m grid (Figure 1a) and depth averaged only over the top 500 m, because this is the modeled region that was best validated with respect to observations. It is noteworthy that the KE reduction is larger in the 2 km HF solution (up to ≈ 40% during summer) if we pick the entire 2 km domain (Supporting Information S1 Energetics), suggesting that the reported values are quite conservative.

The observed reduction in mesoscale KE is a major finding of this study and our goal is to test whether it is induced by IWs. To this end we evaluate the physical-space, temporal scale-to-scale KE transfer rate in all of our solutions using the coarse-graining approach (Aluie et al., 2018; Eyink, 2005; Germano, 1992). This method is advantageous in comparison to the more commonly used spectral methods because it does not require windowing nor the assumptions of homogeneity or isotropy. In addition, the approach is Galilean invariant and therefore less susceptible to doppler-shifting effects and, because it relies on the use of filters in physical space, can also provide structural information about the flow features where the energy transfers take place (e.g., Schubert et al., 2020). A temporal-based analysis is chosen (e.g., Barkan et al., 2017) because the time scales of mesoscale motions and IWs are unambiguously distinguishable, whereas the spatial scales are not.

We compute the coarse-grained KE flux, Π_τ, across a temporal scale τ using (e.g., Aluie et al., 2018)

$$\Pi_\tau(\boldsymbol{x},t) = -\left(\overline{u_i u_j}^\tau - \overline{u_i}^\tau \overline{u_j}^\tau\right)\frac{\partial \overline{u_i}^\tau}{\partial x_j}, \tag{1}$$

where $\overline{()}^\tau$ denotes the width of a low-passed filter applied to the three dimensional velocity field $(u_1,u_2,u_3) = (u,v,w)$; $\boldsymbol{x} = (x_1,x_2,x_3) = (x,y,z)$ is the three dimensional position vector; $i = 1,2$; $j = 1-3$; and summation over repeated indices is assumed. To avoid the edge effects associated with the filtering procedure, the beginning- and end-period corresponding to $1.5\times\tau$ are discarded from the computation. By systematically varying τ we obtain the temporal KE fluxes as a function of filter width, where positive (negative) Π_τ values indicate a forward (inverse) energy transfer across a scale τ. In what follows τ has units of hours and Π_τ is plotted as a function of the equivalent frequency $1/\tau$, so that the coarse-grained KE fluxes can be interpreted in the same way as the more commonly used spectral KE fluxes (e.g., Arbic et al., 2012).

The shape of the depth integrated and horizontally and seasonally averaged Π_τ in all solutions shows that there are scale ranges with both an inverse and a forward energy cascade with intersection periods that vary between ∼1–3 days, depending on the solution (Figures 3a and 3b). A comparison between the SM and HF solutions (solid/dashed black and blue lines in Figures 3a and 3b) demonstrates that IW forcing enhances the forward cascade and reduces the inverse cascade in all cases, where the absolute differences between the HF and SM flux values are as large as the flux magnitudes in the SM solutions. Although a complete scale by scale KE energy balance is beyond the scope of this paper, these large differences in the coarse-grained fluxes plausibly explain the observed reduction in mesoscale KE. There are some variations in Π_τ between the NT and HF solutions, particularly during summer (magenta and black lines in Figure 3b), but qualitatively the induced scale-to-scale flux changes seem to be primarily associated with high-frequency wind forcing and the excitation of NIWs. In most HF solutions there is a local minimum around the inertial frequency (solid red line in Figures 3a and 3b), indicative of a source of NI energy, followed by a local maximum at super-inertial frequencies. This local maximum may be associated with a direct (i.e., non-cascading) KE

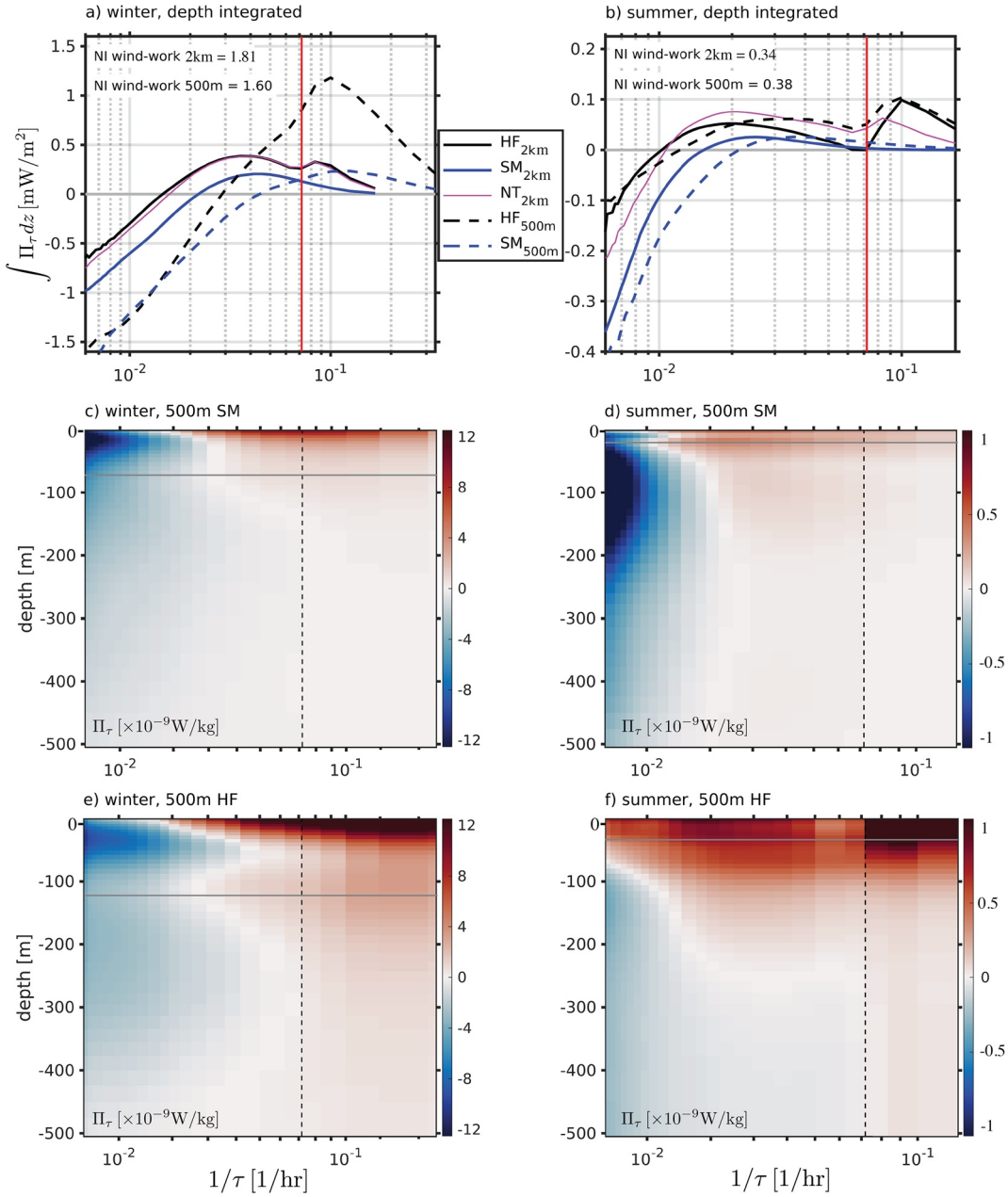

Figure 3. (a and b) Depth integrated (over the top 500 m) and seasonally and horizontally averaged coarse-grained kinetic energy (KE) fluxes, Π_τ, for all numerical simulations described in the text, where temporal filters are computed using a sixth order Butterworth filter. (c–f) The depth structure of the seasonally and horizontally averaged Π_τ for the 500 m solutions. High-frequency forcing (HF) and smooth forcing (SM) denote solutions with and without internal wave (IW) forcing, respectively. No tidal (NT) denotes a solution with high-frequency wind forcing but without tidal forcing. Vertical lines (red in panels a and b and dashed black in panels c–f) denote the inertial frequency. Horizontal gray lines in panels c–f denote the seasonally and horizontally averaged mixed layer depth based on the 0.03 kg/m^3 density criterion (de Boyer Montégut et al., 2004). Horizontal averages are taken over the region occupied by the 500 m grid (Figure 1a). The seasonally and horizontally averaged near-inertial (NI) wind work (in mW/m^2) for the HF 500 m and 2 km solutions are marked in panels (a and b). Note that the *x*-axis range is extended to higher frequencies in the winter plots to better represent the KE flux reduction to zero at the shortest filter widths.

transfer from mesoscale to IW time scales, as suggested by previous theories (e.g., Xie & Vanneste, 2015). At sub-inertial frequencies, however, the externally forced IWs seem to affect the energetics by modifying the turbulent cascades. This cascade-modifying process was termed *stimulated* cascade in Barkan et al. (2017), and was since discussed in Xie (2020) and J. Thomas and Daniel (2021).

Most strikingly, the KE transfer to super-inertial frequencies in the winter 500 m HF solution is substantially larger than that of the winter 500 m SM solution (dashed black and blue lines in Figure 3a), and is on the order of 1mW/m^2. This is comparable to the horizontally averaged NI wind work in this region $\boldsymbol{u}_s^{\text{NI}} \cdot \boldsymbol{\mathcal{T}}^{\text{NI}}$, where $\boldsymbol{u}_s$ is the horizontal surface velocity vector, $\boldsymbol{\mathcal{T}}$ is the surface wind stress vector, and NI denotes a band-pass filter in the $[0.9f, 1.1f]$ frequency band, with f denoting the domain-averaged Coriolis frequency in the 500 m grid. The depth structure of the coarse-grained KE fluxes in the 500 m solutions indicates that transfers are primarily confined to the mixed layer during winter (Figures 3c and 3e), and extend below the mixed layer during summer (Figures 3d and 3f). This suggests that during winter the majority of the transfers may be associated with surface intensified submesoscale currents whereas during summer they are largely linked to mesoscale motions, which typically extend deeper into the thermocline.

4. Flow Structures

The forward KE fluxes to super-inertial frequencies are substantially enhanced during winter in the HF solutions. Theses forward KE fluxes are largely confined to the mixed layer and increase in magnitude with increasing model resolution (Figure 3). Because submesoscale current activity is expected to increase in the mixed layer during winter months (Callies et al., 2015), we hypothesize that submesoscale fronts and filaments, which are better resolved in the 500 m solutions, play an important role in the interactions between eddies and internal wave.

To test this hypothesis we compute the integrated coarse-grained KE fluxes to super-inertial frequencies, Π_{14}, over the top 100 m (Figure 4a), which is roughly the averaged mixed-layer depth during winter in the 500 m HF solution (Figure 3e). Although the signal is somewhat noisy there is a visual correspondence between regions of strong and positive Π_{14} values and regions of strong fronts, which are defined as the ninetieth percentile of the horizontal buoyancy gradient magnitudes $|\nabla_n b|$ ($\approx 1\times10^{-7}\,\text{s}^{-2}$; Figure 4b). Quantitatively, Π_{14} averaged over frontal regions is positive and, in the upper 50 m, nearly an order of magnitude larger than the spatially averaged Π_{14} (Figure 4c).

The frontal-averaged root-mean-squared vorticity and horizontal divergence values normalized by the local Coriolis frequency ($\text{rms}(\zeta/f)$ and $\text{rms}(\delta/f)$) are no longer small in the upper 50 m, indicating a significant departure from geostrophy (Figures 4d and 4e). This dynamical importance of ageostrophic motions is further confirmed by the frontal-averaged skewness values (solid blue lines in Figures 4d and 4e), which are positive (negative) for ζ/f (δ/f), as expected from the circulations around submesoscale fronts and filaments (Barkan et al., 2019; Capet et al., 2008b; D'Asaro et al., 2018; Shcherbina et al., 2013). The importance of the interactions between submesoscale frontal structures and NIWs has been suggested before in theoretical and idealized numerical studies (Barkan et al., 2017; L. N. Thomas, 2012; Whitt & Thomas, 2015), but, to our knowledge, never before demonstrated and quantified in realistic simulations.

5. Implications

The above numerical results and analyses have important implications to dissipation routes of oceanic mesoscale KE and to the energization of NIWs, both of which can significantly affect climate equilibria and biogeochemistry. We offer two approaches to quantify these dissipation and energization processes globally. These approaches assume that the energy transfers in the region of study are representative of other ocean basins, which is difficult to evaluate, and therefore only provide order-of-magnitude estimates.

First, the difference in the magnitudes of the positive KE flux to super-inertial frequencies between the 500 m HF and SM solutions (Figures 3a and 3b) can be multiplied by the surface area of the global world oceans to estimate the IW-induced forward cascade. This gives ~0.35 TW during winter and about a tenth of that during summer.

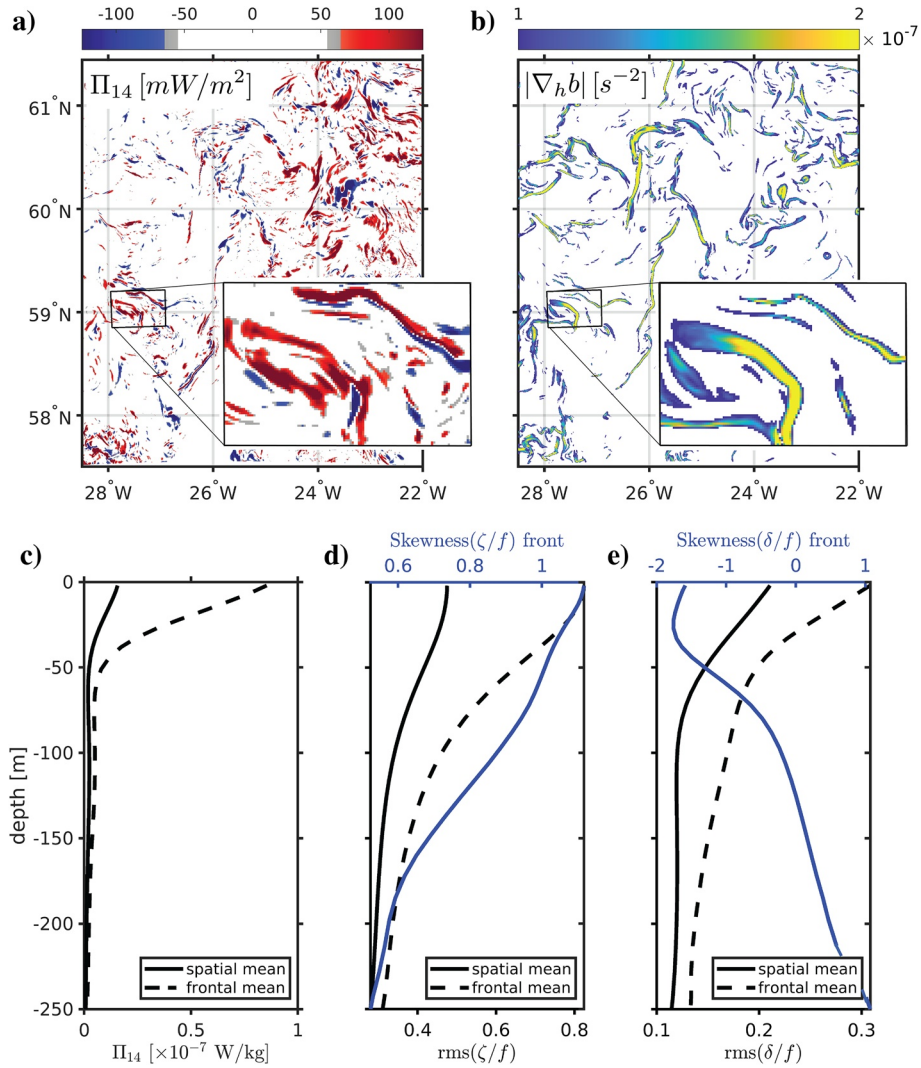

Figure 4. (a) A representative snapshot of the coarse-grained kinetic energy (KE) flux to time scales shorter than 14 h (the inertial period in this region) Π_{14}, depth integrated over the top 100 m. (b) The 90th percentile of the horizontal buoyancy gradient magnitude $|\nabla_h b|$ (i.e., "frontal regions") during the same snapshot as in panel a, low-passed with a 14 h cutoff filter, and depth averaged over the top 100 m. Insets in panels a and b zoom-in on representative structures. Time-mean (c) Π_{14}, (d) root-mean-square vorticity normalized by the Coriolis frequency (rms(ζ/f)), and (e) root-mean-square divergence normalized by the Coriolis frequency (rms(δ/f)), horizontally averaged over the entire 500 m domain (solid black line) and over the "frontal regions" (dashed black line). Blue lines in panels d and e show the skewness of ζ/f and δ/f, respectively, computed in the "frontal regions." All quantities are based on the 500 m high-frequency forcing (HF) solution, during winter.

Second, the same flux magnitude differences between the 500 m HF and SM solutions can be divided by the regionally averaged near-inertial wind work in each season to give the ratio between the super-inertial KE that is transferred from mesoscale motions to that generated by the wind. This ratio is about 0.5–0.6 during winter and 0.18–0.25 during summer. Assuming most of the KE exchanges are associated with NIWs, as indicated by the comparison between HF and NT solutions (Figures 3a and 3b), we multiply these ratios by global estimates of the power input into near-inertial motions, which ranges between 0.3 and 1.3 TW (Alford, 2020; Jiang et al., 2005). This approximates the IW-induced forward cascade to be between 0.05 and 0.8 TW with an annual average of 0.3 TW (based on an assumed 0.8 TW power input into near-inertial motions and an annual-mean ratio of 0.375 between KE flux to super inertial motions and near-inertial wind work). Given that the reduction of low-passed mesoscale energy in the 2 km HF solution is larger when computed over the entire 2 km domain (Supporting Information S1 Energetics) and that the IW-induced

decrease in the inverse KE cascade at sub-inertial frequencies is not taken into consideration in the estimates above, we believe these reported values to be rather conservative.

The strongest forward KE fluxes are found in winter at flow features that are characterized by strong buoyancy gradients and a significant departure from geostrophy (Figure 4). We presume that it is at these submesoscale frontal structures that the KE energy exchanges are most likely to be observed *in situ*.

From a modeling perspective, numerical solutions that exclude IW forcing and/or lack the resolution to adequately resolve the flow structures where the energy transfers occur are expected to over-estimate the low-frequency mesoscale energy by as much as 25%. This over-estimate is comparable in magnitude to the one recently reported for current feedback effects (Renault et al., 2016) and can potentially have significant implications to climate models' predictability, in case they do not adequately represent these "eddy-IW" interactions.

Admittedly, we do not offer here a mechanistic explanation for the stimulated reduction in the inverse KE transfer to sub-inertial frequencies and for the stimulated forward transfer to super-inertial frequencies. Nor do we provide a more in-depth spatiotemporal depiction of the KE energy transfers, following a decomposition between mesoscale, submesoscale, and IW motions. These endeavors are explored in detail in forthcoming publications.

Data Availability Statement

Information about how to access the mooring data can be found in Branellec and Thierry (2016, 2018), at https://archimer.ifremer.fr/doc/00360/47156/ and https://agris.fao.org/agris-search/search.do?recordID=QN2019001268542.

Acknowledgments
Roy Barkan, Kaushik Srinivasan, Luwei Yang, and James C. McWilliams were supported by ONR-N000141812697. Roy Barkan was further supported by NSF Grant OCE-1851397 and Israeli Science foundation Grant 1736/18. James C. McWilliams was further supported ONR-N000141812599 and ONR N000142012023. Jonathan Gula gratefully acknowledges support from the French National Agency for Research (ANR) through the project DEEPER (ANR-19-CE01-0002-01).

References

Alford, M. H. (2003). Redistribution of energy available for ocean mixing by long-range propagation of internal waves. *Nature*, *423*(6936), 159–162. https://doi.org/10.1038/nature01628

Alford, M. H. (2020). Revisiting near-inertial wind work: Slab models, relative stress, and mixed layer deepening. *Journal of Physical Oceanography*, *50*(11), 3141–3156. https://doi.org/10.1175/jpo-d-20-0105.1

Alford, M. H., MacKinnon, J. A., Pinkel, R., & Klymak, J. M. (2017). Space–time scales of shear in the north pacific. *Journal of Physical Oceanography*, *47*(10), 2455–2478. https://doi.org/10.1175/jpo-d-17-0087.1

Alford, M. H., MacKinnon, J. A., Simmons, H. L., & Nash, J. D. (2016). Near-inertial internal gravity waves in the ocean. *Annuel Review of Marine Science*, *8*, 95–123. https://doi.org/10.1146/annurev-marine-010814-015746

Aluie, H., Hecht, M., & Vallis, G. K. (2018). Mapping the energy cascade in the North Atlantic Ocean: The coarse-graining approach. *Journal of Physical Oceanography*, *48*(2), 225–244. https://doi.org/10.1175/jpo-d-17-0100.1

Arbic, B. K., Scott, R. B., Flierl, G. R., Morten, A. J., Richman, J. G., & Shriver, J. F. (2012). Nonlinear cascades of surface oceanic geostrophic kinetic energy in the frequency domain. *Journal of Physical Oceanography*, *42*, 1577–1600. https://doi.org/10.1175/jpo-d-11-0151.1

Arbic, B. K., Shriver, J. F., Hogan, P. J., Hurlburt, H. E., McClean, J. L., Metzger, E. J., & Wallcraft, A. J. (2009). Estimates of bottom flows and bottom boundary layer dissipation of the oceanic general circulation from global high-resolution models. *Journal of Geophysical Research*, *114*. https://doi.org/10.1029/2008jc005072

Barkan, R., Molemaker, M. J., Srinivasan, K., McWilliams, J. C., & D'Asaro, E. A. (2019). The role of horizontal divergence in submesoscale frontogenesis. *Journal of Physical Oceanography*, *49*(6), 1593–1618. https://doi.org/10.1175/jpo-d-18-0162.1

Barkan, R., Winters, K. B., & McWilliams, J. C. (2017). Stimulated imbalance and the enhancement of eddy kinetic energy dissipation by internal waves. *Journal of Physical Oceanography*, *47*, 181–198. https://doi.org/10.1175/jpo-d-16-0117.1

Branellec, P., & Thierry, V. (2016). *Rrex 2015. ctd-o2 data reportODE/LOPS/16-26*. Retrieved from https://archimer.ifremer.fr/doc/00360/47156/

Branellec, P., & Thierry, V. (2018). *Rrex 2017. ctd-o2 data reportRap. Int. LOPS/18-04*. Retrieved from https://agris.fao.org/agris-search/search.do?recordID=QN2019001268542

Bühler, O., & McIntyre, M. E. (2005). Wave capture and wave–vortex duality. *Journal of Fluid Mechanics*, *534*, 67–95. https://doi.org/10.1017/s0022112005004374

Callies, J., Ferrari, R., Klymak, J. M., & Gula, J. (2015). Seasonality in submesoscale turbulence. *Nature Communications*, *6*. https://doi.org/10.1038/ncomms7862

Capet, X., McWilliams, J. C., Molemaker, M. J., & Shchepetkin, A. F. (2008a). Mesoscale to submesoscale transition in the California Current System. Part i: Flow structure, eddy flux, and observational tests. *Journal of Physical Oceangraphy*, *38*, 29–43. https://doi.org/10.1175/2007jpo3671.1

Capet, X., McWilliams, J. C., Molemaker, M. J., & Shchepetkin, A. F. (2008b). Mesoscale to submesoscale transition in the California Current System. Part ii: Frontal processes. *Journal of Physical Oceangraphy*, *38*, 44–64. https://doi.org/10.1175/2007jpo3672.1

Carton, J. A., & Giese, B. S. (2008). A reanalysis of ocean climate using simple ocean data assimilation (soda). *Monthly Weather Review*, *136*(8), 2999–3017. https://doi.org/10.1175/2007mwr1978.1

Chaigneau, A., Pizarro, O., & Rojas, W. (2008). Global climatology of near-inertial current characteristics from Lagrangian observations. *Geophysical Research Letters*, *35*. https://doi.org/10.1029/2008gl034060

D'Asaro, E. A., Shcherbina, A. Y., Klymak, J. M., Molemaker, J., Novelli, G., Guigand, C. M., et al. (2018). Ocean convergence and the dispersion of flotsam. *Proceedings of the National Academy of Sciences*, *115*(6), 1162–1167. https://doi.org/10.1073/pnas.1802701115

de Boyer Montégut, C., Madec, G., Fischer, A. S., Lazar, A., & Iudicone, D. (2004). Mixed layer depth over the global ocean: An examination of profile data and a profile-based climatology. *Journal of Geophysical Research*, *109*(C12). https://doi.org/10.1029/2004jc002378

Dee, D., Balmaseda, M., Balsamo, G., Engelen, R., Simmons, A., & Thépaut, J.-N. (2014). Toward a consistent reanalysis of the climate system. *Bulletin of the American Meteorological Society*, *95*(8), 1235–1248. https://doi.org/10.1175/bams-d-13-00043.1

Egbert, G., & Ray, R. (2000). Significant dissipation of tidal energy in the deep ocean inferred from satellite altimeter data. *Nature*, *405*(6788), 775–778. https://doi.org/10.1038/35015531

Egbert, G. D., Bennett, A. F., & Foreman, M. G. (1994). Topex/poseidon tides estimated using a global inverse model. *Journal of Geophysical Research*, *99*(C12), 24821–24852. https://doi.org/10.1029/94jc01894

Egbert, G. D., & Erofeeva, S. Y. (2002). Efficient inverse modeling of barotropic ocean tides. *Journal of Atmospheric and Oceanic Technology*, *19*(2), 183–204. https://doi.org/10.1175/1520-0426(2002)019<0183:eimobo>2.0.co;2

Eyink, G. L. (2005). Locality of turbulent cascades. *Physica D: Nonlinear Phenomena*, *207*(1–2), 91–116. https://doi.org/10.1016/j.physd.2005.05.018

Fratantoni, D. M. (2001). North Atlantic surface circulation during the 1990's observed with satellite-tracked drifters. *Journal of Geophysical Research*, *106*, 22067–22093. https://doi.org/10.1029/2000jc000730

Germano, M. (1992). Turbulence- the filtering approach. *Journal of Fluid Mechanics*, *238*(1), 325–336. https://doi.org/10.1017/s0022112092001733

Jakobsen, P. K., Ribergaard, M. H., Quadfasel, D., Schmith, T., & Hughes, C. W. (2003). Near-surface circulation in the northern North Atlantic as inferred from Lagrangian drifters: Variability from the mesoscale to interannual. *Journal of Geophysical Research*, *108*. https://doi.org/10.1029/2002jc001554

Jiang, J., Lu, Y., & Perrie, W. (2005). Estimating the energy flux from the wind to ocean inertial motions: The sensitivity to surface wind fields. *Geophysical Research Letters*, *32*(15). https://doi.org/10.1029/2005gl023289

Jochum, M., Briegleb, B. P., Danabasoglu, G., Large, W. G., Norton, N. J., Jayne, S. R., et al. (2013). The impact of oceanic near-inertial waves on climate. *Journal of Climate*, *26*(9), 2833–2844. https://doi.org/10.1175/jcli-d-12-00181.1

McWilliams, J. C. (2016). Submesoscale currents in the ocean. *Proceedings of the Royal Society A: Mathematical, Physical and Engineering Sciences*, *125*, 20160117. https://doi.org/10.1098/rspa.2016.0117

Müller, P., McWilliams, J. C., & Molemaker, M. J. (2005). Routes to dissipation in the ocean: The 2d/3d turbulence conundrum. In H. B. J. Simpson, & J. Sündermann (Eds.), Marine turbulence (pp. 397–405). Cambridge University Press.

Nelson, A., Arbic, B., Menemenlis, D., Peltier, W., Alford, M., Grisouard, N., & Klymak, J. (2020). Improved internal wave spectral continuum in a regional ocean model. *Journal of Geophysical Research: Oceans*, *125*(5), e2019JC015974. https://doi.org/10.1029/2019jc015974

Nikurashin, M., Vallis, G. K., & Adcroft, A. (2013). Routes to energy dissipation for geostrophic flows in the southern ocean. *Nature Geoscience*, *6*, 48–51. https://doi.org/10.1038/ngeo1657

Pinkel, R. (2014). Vortical and internal wave shear and strain. *Journal of Physical Oceanography*, *44*, 2070–2092. https://doi.org/10.1175/jpo-d-13-090.1

Polzin, K. L. (2010). Mesoscale eddy-internal wave coupling. part ii: Energetics and results from polymode. *Journal of Physical Oceanography*, *40*(4), 789–801. https://doi.org/10.1175/2009jpo4039.1

Renault, L., Molemaker, M. J., McWilliams, J. C., Shchepetkin, A. F., Lemarié, F., Chelton, D., et al. (2016). Modulation of wind work by oceanic current interaction with the atmosphere. *Journal of Physical Oceanography*, *46*, 1685–1704. https://doi.org/10.1175/jpo-d-15-0232.1

Rocha, C. B., Wagner, G. L., & Young, W. R. (2018). Stimulated generation: Extraction of energy from balanced flow by near-inertial waves. *Journal of Fluid Mechanics*, *847*, 417–451. https://doi.org/10.1017/jfm.2018.308

Schubert, R., Gula, J., Greatbatch, R. J., Baschek, B., & Biastoch, A. (2020). The submesoscale kinetic energy cascade: Mesoscale absorption of submesoscale mixed layer eddies and frontal downscale fluxes. *Journal of Physical Oceanography*, *50*(9), 2573–2589. https://doi.org/10.1175/jpo-d-19-0311.1

Sen, A., Scott, R. B., & Arbic, B. K. (2008). Global energy dissipation rate of deep-ocean low-frequency flows by quadratic bottom boundary layer drag: Computations from current-meter data. *Geophysical Research Letters*, *35*. https://doi.org/10.1029/2008gl033407

Shchepetkin, A. F., & McWilliams, J. C. (2005). The regional oceanic modeling system: A split-explicit, free-surface, topography-following-coordinate oceanic model. *Ocean Modelling*, *9*, 347–404. https://doi.org/10.1016/j.ocemod.2004.08.002

Shcherbina, A. Y., D'Asaro, E. A., Lee, C. M., Klymak, J. M., Molemaker, M. J., & McWilliams, J. C. (2013). Statistics of vertical vorticity, divergence, and strain in a developed submesoscale turbulence field. *Geophysical Research Letters*, *40*, 4706–4711. https://doi.org/10.1002/grl.50919

Taylor, S., & Straub, D. (2016). Forced near-inertial motion and dissipation of low-frequency kinetic energy in a wind-driven channel flow. *Journal of Physical Oceanography*, *46*(1), 79–93. https://doi.org/10.1175/jpo-d-15-0060.1

Taylor, S., & Straub, D. (2020). Effects of adding forced near-inertial motion to a wind-driven channel flow. *Journal of Physical Oceanography*, *50*(10), 2983–2996. https://doi.org/10.1175/jpo-d-19-0299.1

Thomas, J., & Daniel, D. (2020). Turbulent exchanges between near-inertial waves and balanced flows. *Journal of Fluid Mechanics*, *902*. https://doi.org/10.1017/jfm.2020.510

Thomas, J., & Daniel, D. (2021). Forward flux and enhanced dissipation of geostrophic balanced energy. *Journal of Fluid Mechanics*, *911*. https://doi.org/10.1017/jfm.2020.1026

Thomas, L., Rainville, L., Asselin, O., Young, W. R., Girton, J., Whalen, C. B., & Hormann, V. (2020). Direct observations of near-inertial wave ζ- refraction in a dipole vortex. *Geophysical Research Letters*, *47*(21), e2020GL090375. https://doi.org/10.1029/2020gl090375

Thomas, L. N. (2012). On the effects of frontogenetic strain on symmetric instability and inertia-gravity waves. *Journal of Fluid Mechanics*, *711*, 620–640. https://doi.org/10.1017/jfm.2012.416

Thomas, L. N. (2017). On the modifications of near-inertial waves at fronts: Implications for energy transfer across scales. *Ocean Dynamics*, *67*(10), 1335–1350. https://doi.org/10.1007/s10236-017-1088-6

Trossman, D. S., Arbic, B. K., Garner, S. T., Goff, J. A., Jayne, S. R., Metzger, E. J., & Wallcraft, A. J. (2013). Impact of parameterized lee wave drag on the energy budget of an eddying global ocean model. *Ocean Modelling*, *72*, 119–142. https://doi.org/10.1016/j.ocemod.2013.08.006

Trossman, D. S., Arbic, B. K., Richman, J. G., Garner, S. T., Jayne, S. R., & Wallcraft, A. J. (2016). Impact of topographic internal lee wave drag on an eddying global ocean model. *Ocean Modelling*, *97*, 109–128. https://doi.org/10.1016/j.ocemod.2015.10.013

Vic, C., Ferron, B., Thierry, V., Mercier, H., & Lherminier, P. (2021). Tidal and near-inertial internal waves over the Reykjanes Ridge. *Journal of Physical Oceanography*, *51*(2), 419–437. https://doi.org/10.1175/jpo-d-20-0097.1

Wagner, G., & Young, W. (2016). A three-component model for the coupled evolution of near-inertial waves, quasi-geostrophic flow, and the near-inertial second harmonic. *Journal of Fluid Mechanics*, *11*, 1111. https://doi.org/10.1017/jfm.2016.487

Whitt, D. B., & Thomas, L. N. (2015). Resonant generation and energetics of wind-forced near-inertial motions in a geostrophic flow. *Journal of Physical Oceanography*, *45*(1), 181–208. https://doi.org/10.1175/jpo-d-14-0168.1

Wunsch, C., & Ferrari, R. (2004). Vertical mixing, energy, and the general circulation of the oceans. *Annual Review of Fluid Mechanics*, *36*, 281–314. https://doi.org/10.1146/annurev.fluid.36.050802.122121

Xie, J.-H. (2020). Downscale transfer of quasigeostrophic energy catalyzed by near-inertial waves. *Journal of Fluid Mechanics*, *904*, A40. https://doi.org/10.1017/jfm.2020.709

Xie, J.-H., & Vanneste, J. (2015). A generalised-Lagrangian-mean model of the interactions between near-inertial waves and mean flow. *Journal of Fluid Mechanics*, *774*, 143–169. https://doi.org/10.1017/jfm.2015.251

References From the Supporting Information

Argo. (2000). Argo float data and metadata from global data assembly centre (argo gdac). SEANOE.

C3S, C. C. C. S. (2017). *Era5: Fifth generation of ecmwf atmospheric reanalyses of the global climate*. Copernicus Climate Change Service Climate Data Store. (CDS).

Ducet, N., Le Traon, P.-Y., & Reverdin, G. (2000). Global high-resolution mapping of ocean circulation from topex/poseidon and ers-1 and-2. *Journal of Geophysical Research*, *105*(C8), 19477–19498. https://doi.org/10.1029/2000jc900063

Gaillard, F., Reynaud, T., Thierry, V., Kolodziejczyk, N., & Von Schuckmann, K. (2016). In situ–based reanalysis of the global ocean temperature and salinity with ISAS: Variability of the heat content and steric height. *Journal of Climate*, *29*(4), 1305–1323. https://doi.org/10.1175/jcli-d-15-0028.1

Kolodziejczyk Nicolas, G. F., & Annaig, P.-M. (2021). *ISAS temperature and salinity gridded fields*. SEANOE.

Large, W., & Yeager, S. (2009). The global climatology of an interannually varying air–sea flux data set. *Climate Dynamics*, *33*, 341–364. https://doi.org/10.1007/s00382-008-0441-3

Large, W. B. (2006). Surface fluxes for practitioners of global ocean data assimilation. In Ocean weather forecasting (pp. 229–270). Springer.

Large, W. G., McWilliams, J. C., & Doney, S. C. (1994). Oceanic vertical mixing: A review and a model with a nonlocal boundary layer parameterization. *Reviews of Geophysics*, *32*, 363–403. https://doi.org/10.1029/94rg01872

Le Corre, M., Gula, J., & Tréguier, A.-M. (2020). Barotropic vorticity balance of the north Atlantic subpolar gyre in an eddy-resolving model. *Ocean Science*, *16*(2), 451–468. https://doi.org/10.5194/os-16-451-2020

Lemarié, F., Kurian, J., Shchepetkin, A. F., Molemaker, M. J., Colas, F., & McWilliams, J. C. (2012). Are there inescapable issues prohibiting the use of terrain-following coordinates in climate models? *Ocean Modelling*, *42*, 57–79. https://doi.org/10.1016/j.ocemod.2011.11.007

Mason, E., Molemaker, J., Shchepetkin, A. F., Colas, F., McWilliams, J. C., & Sangrà, P. (2010). Procedures for offline grid nesting in regional ocean models. *Ocean Modelling*, *35*, 1–15. https://doi.org/10.1016/j.ocemod.2010.05.007

Renault, L., Masson, S., Arsouze, T., Madec, G., & Mcwilliams, J. C. (2020). Recipes for how to force oceanic model dynamics. *Journal of Advances in Modeling Earth Systems*, *12*(2), e2019MS001715. https://doi.org/10.1029/2019ms001715

Shchepetkin, A. F. (2015). An adaptive, courant-number-dependent implicit scheme for vertical advection in oceanic modeling. *Ocean Modelling*, *91*, 38–69. https://doi.org/10.1016/j.ocemod.2015.03.006

Shchepetkin, A. F., & McWilliams, J. C. (2011). Accurate Boussinesq oceanic modeling with a practical, "stiffened" equation of state. *Ocean Modelling*, *38*, 41–70. https://doi.org/10.1016/j.ocemod.2011.01.010

Smilenova, A., Gula, J., Le Corre, M., Houpert, L., & Reecht, Y. (2020). A persistent deep anticyclonic vortex in the rockall trough sustained by anticyclonic vortices shed from the slope current and wintertime convection. *Journal of Geophysical Research: Oceans*, *125*(10), e2019JC015905. https://doi.org/10.1029/2019jc015905